International Journal of Solids and Structures 115–116 (2017) 270–278

Contents lists available at ScienceDirect

International Journal of Solids and Structures

journal homepage: www.elsevier.com/locate/ijsolstr

Finite element simulation of single crystal and polycrystalline Haynes 230 specimens

P.G. Luccarelli[a,*], G.J. Pataky[b], H. Sehitoglu[c], S. Foletti[a]

[a] Department of Mechanical Engineering, Politecnico di Milano, Via La Masa 1, 20156 Milan, Italy
[b] Department of Mechanical Engineering, Clemson University, 29634 Clemson, SC, USA
[c] Department of Mechanical Science and Engineering, University of Illinois at Urbana-Champaign, 1206 W Green Street, 61801 Urbana, IL, USA

ARTICLE INFO

Article history:
Received 20 July 2016
Revised 16 November 2016
Available online 23 March 2017

Keywords:
Single crystal
Polycrystalline media
Nickel-based alloy
3D Finite element analysis
Crystal plasticity

ABSTRACT

Metallic materials are typically described on the macroscopic scale without consideration that they are an aggregate of grains at the micro scale. Taking this into account, finite element simulations with a crystal plasticity model were used to reproduce the behavior of a Nickel-based superalloy, Haynes 230. The aim of this work was to replicate the local behavior of a real polycrystalline aggregate. The simulation was constructed based on the microstructure of a Haynes 230 sample, obtained via electron backscatter diffraction. Utilizing digital image correlation during the experiment provided the opportunity to directly compare the simulation and experimental results. The present paper includes a description of the numerical model used for the analysis, its application to tensile experiments conducted on single crystal specimens and finally to a polycrystalline specimen. The validation of the results was based on the macro scale behavior of the tensile tests curves and on the local strain accumulation occurring in the grains and along grain boundaries.

1. Introduction

The analysis of the effective plastic behavior in polycrystalline materials by means of Finite Element (FE) is of considerable interest (Marin and Dawson, 1998; Zbib and de la Rubia, 2002; Xie et al., 2004; Diard et al., 2005). Plastic deformation in metals is a very complex phenomenon originating from highly nonlinear dynamical processes associated with microscopic defects, such as dislocations, voids and micro cracks. Assuming the absence of internal defects, dislocations and their mutual interaction determine the material strength. They tend to self-organize in patterns (Aifantis, 1995) with the results forming a heterogeneous field of deformation at the micro scale although the macro-level is thought to be homogeneous. Constitutive models formulated using the concept of Crystal Plasticity (CP) aim to estimate the response of mesoscale deformations by representing shear deformations along discrete crystallographic slip systems.

The implementation of CP models in FE codes is of priority to further physics-based modeling efforts. Warp3D, an open-source finite element solver, incorporates a physically based CP model (Asaro, 1983) to represent the response of individual grain. The CP model accounts for the kinematics of the lattice deformation and a constitutive relation for the slip system response, which is able to link shear strain rates and stresses on slip planes (Healy et al., 2015). The investigation of CP finite element modeling is well pursued in Barbe et al. (2001a, 2001b); Musienko et al. (2007) where the main objectives are the study at the micro scale level of a random generated polycrystal (Barbe et al., 2001a, 2001b) and the representative response at the macro scale (Musienko et al., 2007). Further analysis are focused on showing at the micro scale the discontinuity between grains in terms of stresses and strains.

In the current paper, we combine modeling efforts with experimental observations in order to investigate the material behavior and the parameters governing the FE models. By means of Digital Image Correlation (DIC) techniques, single crystal and polycrystalline specimens were analyzed for their overall response (in terms of stress-strain curves) and strain localizations across grains and grain boundaries. The results were used as a feedback to calibrate the constitutive model. The material studied is the Nickel-based superalloy Haynes 230, an alloy that, due to its high strength and good oxidation resistance, is being used in afterburner parts in current gas turbine engines (Lu et al., 2005).

Using the crystallographic orientations of the single crystal specimens and the Electron Backscatter Diffraction (EBSD) map of a polycrystalline specimen, the behavior of the material was modeled by means of a crystal plasticity FE code. The analysis

* Corresponding author.
E-mail address: pietrogiovanni.luccarelli@polimi.it (P.G. Luccarelli).

http://dx.doi.org/10.1016/j.ijsolstr.2017.03.025
0020-7683/

Nomenclature

C	Elastic stiffness tensor
D_0, T_0, μ_0	Empirical parameters for temperature dependent shear modulus
E, ν	Young's modulus and Poisson's ratio
F, F^e, F^p	Deformation gradient and its elastic and plastic components
L, D, W	Velocity gradient and its symmetric and skew components
$\bar{L}^p$, $\bar{D}^p$, $\bar{W}^p$	Plastic velocity gradient and its symmetric and skew components
T	Temperature
b	Burgers vector's magnitude
$b^{(s)}$	Direction of the sth slip system
g_0	Normalized activation energy
k	Boltzman constant
k_0, k_1	Parameters characterizing the work hardening
m	Schmid factor
n	Exponent of the slip rate
n_{slip}	Number of slip systems
$n^{(s)}$	Normal of the sth slip system
q_i, p_i	Statistical constant to characterize energy barriers
s	S th slip system
α	Nye tensor
$\dot{\gamma}^0$	Reference slip rate
$\dot{\gamma}^{(s)}$	Slip rate along the sth slip system
$\dot{\epsilon}_0$	Reference strain rate
ϑ_0	Initial slope of the work hardening
$\lambda^{(s)}$	Geometric dislocation density
μ	Shear modulus
ξ	Elastic strain
ρ	Geometrically necessary dislocation density
σ_{remote}	Remote applied stress
τ	Shear stress
$\tau^{(s)}$	Resolved shear stress on the sth slip system
$\tilde{\tau}$	Slip system strength
$\hat{\tau}_a$	Temperature and rate invariant component of the yield stress
$\hat{\tau}_y$	Temperature and rate dependent component of the yield stress
$\hat{\tau}_v$	Saturation strength of the work hardening
$\bar{\tau}$	Slip system strength component that account for work hardening

will compare experiments and simulations in order to evaluate the agreement between the two results. Further modeling efforts introducing carbides in the polycrystalline matrix, identified by micro structural analysis, lead to a better comprehension of the DIC results.

2. Crystal plasticity model

The crystal plasticity model used in this work is based on an elasitc-plastic formulation (Asaro, 1983; Healy et al., 2015): the kinematics of a crystal are a combination of dislocation slip, lattice rotation and elastic stretch; Fig. 1 illustrates the multiplicative decomposition used for the deformation gradient, originally proposed by Lee (1969):

$$F = F^e F^p = V^e R^e F^p = (I + \xi) R^e F^p \tag{1}$$

F^e is the elastic deformation gradient that accounts for stretching (V^e) and lattice rotation (R^e). The stretching can be written as

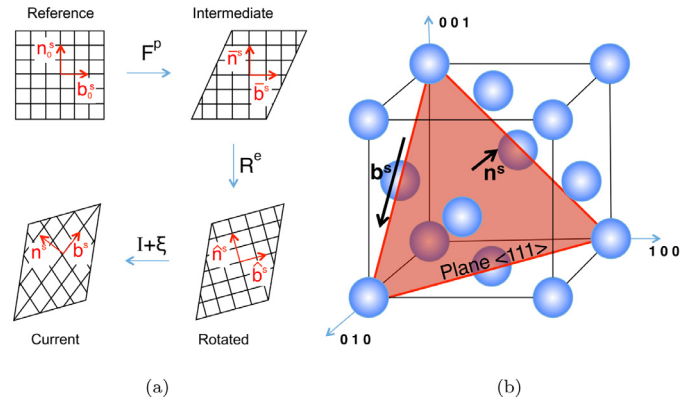

Fig. 1. a) Schematic of the decomposition for the kinematics of the elastic-plastic deformation in a crystal; b) slip systems definition inside an FCC crystal lattice.

$(I + \xi)$ where I is the unit matrix and ξ is a small variation; under high plastic strain condition, elastic strain can be considered small so that $||\xi|| \ll 1$. F^p is the plastic deformation gradient that accounts for slip. In Fig. 1, $b^{(s)}$ and $n^{(s)}$ are, respectively, the unit vector in the slip direction and the unit normal vector to the slip plane of the sth system. Those are represented for every multiplicative step with the respective notation. From Eq. (1), the velocity gradient L in the current configuration is defined using the standard formulation as:

$$L = \dot{F} F^{-1} = \dot{F}^e F^{e^{-1}} + F^e \dot{F}^p F^{p^{-1}} F^{e^{-1}} = \dot{F}^e F^{e^{-1}} + F^e \bar{L}^p F^{e^{-1}} \tag{2}$$

$\bar{L}^p = \dot{F}^p F^{p^{-1}}$ is defined as a constitutive tensor, which represents the plastic velocity gradient with respect to the intermediate configuration. Expressing $L = D + W$ (Roters et al., 2010) as the sum of the skew $W = 1/2\left(L - L^T\right)$ and the symmetric $D = 1/2\left(L + L^T\right)$ components. Combining Eqs. (1) and (2), the following relations can be derived:

$$D = \dot{\xi} + \hat{D}^p + \xi \hat{W}^p - \hat{W}^p \xi - \frac{1}{2}\left(\xi \dot{\xi} + \dot{\xi} \xi\right) \tag{3}$$

$$W = \hat{W}^p + \xi \hat{D}^p - \hat{D}^p \xi + \frac{1}{2}\left(\xi \dot{\xi} - \dot{\xi} \xi\right) \tag{4}$$

$$\hat{D}^p = R^e \bar{D}^p R^{e^T} \quad \hat{W}^p = \dot{R}^e R^{e^T} + R^e \bar{W}^p R^{e^T} \tag{5}$$

$\bar{D}^p$ and $\bar{W}^p$ can be obtained from the plastic velocity gradient. Considering a single crystal and assuming that all the plastic straining is correlated to the slip on slip planes, $\bar{L}^p$ can be expressed as an additive decomposition of plastic shear deformation in a lattice frame (Healy et al., 2015):

$$\bar{L}^p = \sum_{s=1}^{n_{slip}} \dot{\gamma}^{(s)} \left(\bar{b}^{(s)} \otimes \bar{n}^{(s)}\right) \tag{6}$$

where $\bar{b}^{(s)}$ and $\bar{n}^{(s)}$ are related to the intermediate configuration and $\dot{\gamma}^{(s)}$ is the slip rate along each slip system. $\bar{L}^p$ can be decomposed into its skew and symmetric components:

$$\bar{D}^p = \sum_{s=1}^{n_{slip}} \dot{\gamma}^{(s)} \left(\bar{b}^{(s)} \otimes \bar{n}^{(s)}\right)_{sym} \qquad \left(\bar{b}^{(s)} \otimes \bar{n}^{(s)}\right)_{sym} = \frac{1}{2}\left(\bar{b}^{(s)} \otimes \bar{n}^{(s)} + \bar{n}^{(s)} \otimes \bar{b}^{(s)}\right) \tag{7}$$

$$\bar{W}^p = \sum_{s=1}^{n_{slip}} \dot{\gamma}^{(s)} \left(\bar{b}^{(s)} \otimes \bar{n}^{(s)}\right)_{asym} \qquad \left(\bar{b}^{(s)} \otimes \bar{n}^{(s)}\right)_{asym} = \frac{1}{2}\left(\bar{b}^{(s)} \otimes \bar{n}^{(s)} - \bar{n}^{(s)} \otimes \bar{b}^{(s)}\right) \tag{8}$$

Considering Eq. (3), under the hypothesis of small elastic strains, it is possible to introduce the relationship: $C\dot{\xi} = \dot{\tau}$,

with C as the elastic stiffness tensor. Eq. (3), neglecting the effects of the quadratic terms in $\dot{\xi}$ and ξ, becomes $CD = \dot{\tau} + \tau\hat{W}^p + C\hat{D}^p - \hat{W}^p\tau$, which can be used to determine the shear stress rate for the FEM integration:

$$\dot{\tau} = C_0\left(D - \hat{D}^p\right) - \tau\hat{W}^p + \hat{W}^p\tau \tag{9}$$

where C_0 is the stiffness matrix in the reference configuration (Fig. 1).

The slip rate is taken as a power law on a reference strain rate, the resolved shear stress and slip system strength. In the considered model the slip system hardening is isotropic; all slip systems have the same strength. The relation for the slip rate is:

$$\dot{\gamma}^{(s)} = \frac{\dot{\gamma}^0}{\tilde{\tau}}\left|\frac{\tau^{(s)}}{\tilde{\tau}}\right|^{n-1}\tau^{(s)} \tag{10}$$

with $\dot{\gamma}^0$ as the reference slip rate, $\tilde{\tau}$ as the slip system strength and $\tau^{(s)}$ as the resolved shear stress on the slip system s. In Eq. (10) a relationship for the slip system strength is still missing. A constitutive model to describe it has to be defined. The model used to describe the material hardening is a physically based one; it relies on dislocation density to describe plastic deformations (Roters et al., 2010).

The Mechanical Threshold Stress (MTS) model (Healy et al., 2015; Kok et al., 2002b) is an isotropic scalar model that predicts flow stress as a function of strain rate, temperature and current state. It has been used successfully in the analysis of various materials (Banerjee, 2007; Follansbee, 2014; Goto et al., 2000). The mechanical threshold, $\hat{\tau}_{MTS}$, is defined as the flow shear stress at $0K$ and is separated in an athermal component $\hat{\tau}_a$ and thermal components $\tilde{\tau}_i$:

$$\tilde{\tau}(T,\dot{\epsilon}_p) = \hat{\tau}_{MTS} = \hat{\tau}_a + \sum_{i=1}^{m_i}\tilde{\tau}_i \tag{11}$$

$\hat{\tau}_a$ characterizes the rate-independent interaction with thermal barriers; $\tilde{\tau}_i$ characterizes the interaction of dislocations with obstacles where strain rate and thermal activation assist to overcome the obstacles (Follansbee and Kocks, 1988); $i = 1 : m_i$ identifies the number of thermal components to be used for the model. The flow stress for all the slip systems of a single crystal is expressed as:

$$\tilde{\tau}(T,\dot{\epsilon}_p) = \hat{\tau}_{MTS} = \hat{\tau}_a + \frac{\mu(T)}{\mu_0}\sum_{i=1}^{m_i}S_i(T,\dot{\epsilon}_p)\,\hat{\tau}_i \tag{12}$$

where μ/μ_0 accounts for the temperature dependent elastic properties of the material:

$$\mu(T) = \mu_0 - \frac{D_0}{\exp\left(\frac{T_0}{T}\right) - 1} \tag{13}$$

μ_0 is a reference value for the shear modulus and T_0 and D_0 are empirical constants.

It is possible to express the scaling factor S_i considering an Arrhenius type equation to describe interaction kinetics for short-range obstacles and a phenomenological relation for the free energy function of stress (Kocks, 1975; Kocks and Mecking, 2003):

$$\tilde{\tau}_i = S_i(T,\dot{\epsilon}_p)\,\hat{\tau}_i = \left[1 - \left(\frac{kT}{g_{0,i}\,\mu\,b^3}\ln\frac{\dot{\epsilon}_{0,i}}{\dot{\epsilon}_p}\right)^{\frac{1}{q_i}}\right]^{\frac{1}{p_i}}\hat{\tau}_i \tag{14}$$

Where for the ith component the following parameters have to be identified: k is the Boltzman constant; b is the magnitude of the Burgers vector: $g_{0,i}$ is the normalized activation energy for dislocation to overcome the obstacles; $\dot{\epsilon}_{0,i}\dot{\epsilon}_{0,i}$ is a constant; p_i and q_i are statistical constants that characterize the shape of the obstacle profile; $\dot{\epsilon}$ can be evaluated as $\dot{\epsilon}_p = \sqrt{\frac{2}{3}D : D}$; $\hat{\tau}_i$ is a scalar representing the strength of the ith component.

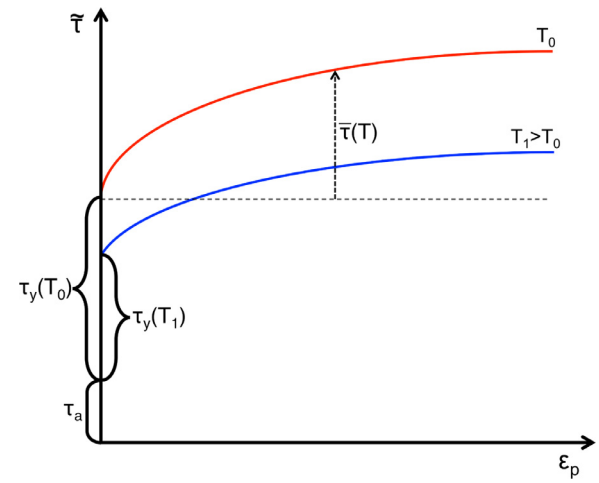

Fig. 2. Schematic of the MTS hardening model with highlights of the major parameters describing it.

To complete the work hardening model of Eq. (12), two terms of the type shown in Eq. (14) are considered, $m_i = 2$, one representing all intrinsic barrier to dislocation motion and one all work hardening. This general form reproduces the behavior shown in Fig. 2, considering the initial strength to dislocation motion (yielding) and the subsequent increasing due to dislocation hardening (Kok et al., 2002b). The terms in Eq. (12) have the form:

$$\tilde{\tau}(T,\dot{\epsilon}_p) = \hat{\tau}_a + \tilde{\tau}_y(T,\dot{\epsilon}_p)\frac{\mu}{\mu_0} + \bar{\tau}(\tilde{\tau}_v(T,\dot{\epsilon}_p))\frac{\mu}{\mu_0} \tag{15}$$

Where $\bar{\tau}$ can be evaluated in its rate form, following the Voce law:

$$\dot{\bar{\tau}} = \vartheta_0\left[1 - \frac{\bar{\tau}}{\tilde{\tau}_v}\right]\sum_{s=1}^{n_{slip}}\dot{\gamma}^{(s)} \tag{16}$$

ϑ_0 is the initial slope of the work hardening curve of Fig. 2; $\sum_{s=1}^{n_{slip}}\dot{\gamma}^{(s)}$ represents the plastic strain rate; $\tilde{\tau}_v$ follows the law of Eq. (14) and represents the work hardening strength. In Eq. (15) the two terms that follows the Arrhenius type formulation are:

$$\tilde{\tau}_y = S_y(T,\dot{\epsilon}_p)\hat{\tau}_y \quad \tilde{\tau}_v = S_v(T,\dot{\epsilon}_p)\hat{\tau}_v \tag{17}$$

In addition to the terms in Eq. (16) it is possible to also account for geometrically necessary dislocations and evaluate the Nye tensor (Nye, 1953) and the dislocation density:

$$\alpha = -\nabla\times F^{e^{-1}} \quad \lambda^{(s)} = \sqrt{(\alpha\bar{n}^{(s)}) : (\alpha\bar{n}^{(s)})} \tag{18}$$

It is possible to add a term in Eq. (16) (Acharya et al., 2003):

$$\tau_\lambda^{(s)} = \frac{k_0}{k_1}\eta\,\mu\,\lambda^{(s)} \tag{19}$$

where $k_1 = 2\vartheta_0/\eta\mu b$ and k_0 is a parameter characterizing the stage IV of the work hardening (Kok et al., 2002a); so Eq. (16) can be modified adding a normalized term:

$$\dot{\bar{\tau}} = \sum_{s=1}^{n_{slip}}\vartheta_0\left[1 - \frac{\bar{\tau}}{\tilde{\tau}_v} + \frac{\tau_\lambda^{(s)}}{\bar{\tau}}\right]\dot{\gamma}^{(s)} \tag{20}$$

The $\tau_\lambda^{(s)}$ influences the work hardening plastic deformation (for low deformation its value is very small, so it practically affects only the final stage of the work hardening which has a nearly constant hardening slope).

3. Experiments

DIC was utilized for measuring global and local displacement for both the single crystal and the polycrystalline specimens.

Table 1
Material parameters for crystal plasticity simulation of Haynes 230 single crystals.

Property	Description	Fitting/Literature	Value
E	Young's modulus	Fitted	218 GPa
ν	Poisson's ratio	Fitted	0.33
μ_0	Shear modulus	Fitted	89.5 GPa
n	Exponent of the slip rate	Fitted	20
b	Burgers Vector	Literature (Gray III et al., 1999)	$2.5E-7$ mm
$\hat{\tau}_a$	Athermal slip resistence	Literature (Healy et al., 2015)	0 MPa
$\hat{\tau}_y$	MTS strength for intrinsic barrier (yield)	Fitted	130 MPa
$g_{0,y}$	Normalized activation energy for intrinsic barriers	Literature (Gray III et al., 1999)	0.37
q_y	Shape coefficient for intrinsic barriers	Literature (Kok et al., 2002b)	1.5
p_y	Shape coefficient for intrinsic barriers	Literature (Kok et al., 2002b)	1.5
$\epsilon_{0,y}$	Strain rate sensitivity for intrinsic barriers	Literature (Banerjee, 2007)	$1E9$ s $^{-1}$
$\hat{\tau}_v$	MTS strength for work hardening	Fitted	80 MPa
$g_{0,v}$	Normalized activation energy for work hardening	Literature (Gray III et al., 1999)	1.6
q_v	Shape coefficient for work hardening	Literature (Kok et al., 2002b)	0.667
p_v	Shape coefficient for work hardening	Literature (Kok et al., 2002b)	1.2
$\epsilon_{0,v}$	Strain rate sensitivity for work hardening	Literature (Banerjee, 2007)	$1E7$ s $^{-1}$
ϑ_0	Initial hardening slope	Fitted	110 MPa
k_0	Geometric hardening parameter	Fitted	1

The single crystal specimens were grown using the Bridgman technique in vacuum and orientations verified using EBSD: the three tested specimens were oriented with the [001], [011], [111] directions along the loading direction. Dog-bone tension specimens were electrical discharge machined (EDM) with a gage length of 9 mm, a width of 3 mm, and a thickness of approximately 1 mm. The specimens were mechanically polished to a mirror finish, and then the speckle pattern was airbrushed onto each specimen using black paint. Monotonic tension experiments were performed in a servo-hydraulic load frame capturing deformation images *in-situ* at a rate of 15 fps until failure. DIC images were captured with a field of view of 2.9 mm by 2.6 mm with a resolution of 2.2 μm/pixel. Correlation was performed with the following parameters: subset size 134 μm (61 px), step size of 11 μm (5 px), and a strain window of 5. A spatial resolution of 178 μm was used for determining the strain fields as defined in Reu (2015).

The polycrystalline specimen was larger to accommodate induction heating coils as experiment was performed at 700 °C. The specimen dimension were length of 25 mm gage, width of 4 mm, and thickness of 2.38 mm. EBSD was performed on an area of 0.5 mm by 1 mm before the experiment. DIC images were captured *ex-situ* with an optical microscope to improve spatial resolution. Due to this, the experiment was performed as an interrupted monotonic tension experiment. Full details can be found in Pataky and Sehitoglu (2015). Images were captured at a resolution of 0.175 μm and correlations were performed with a subset size of 8.9 μm (51 px), step size of 0.875 μm (5 px) and a strain window of 5. This corresponded to a spatial resolution of 12.425 μm.

4. Crystal plasticity model parameters identification

To complete the analysis of the FE models, it is necessary for the material parameters to be identified; the analysis of single crystal experiments permits an iterative optimization. Then the identified parameters were used to reproduce one of the single crystal tests local behavior.

4.1. Material parameters identification

To simulate the single crystal experimental stress-strain curves, a cubic representative volume was adopted with load orientations along the [001], [011] and [111] directions. The simulation were processed considering a cubic geometry of 1 × 1 × 1 mm and 1000 hexahedral linear elements. Each element was associated with the Euler angles corresponding to the specimen's orientation. The load was applied as a displacement, like the experiment, on one face of the cube while the opposing face was displacement constraint along the load direction. For these models, only the overall behavior in stress-strain was analyzed. The comparison between the stress-strain curves of the three simulations and the experiments, Fig. 3, highlighted a good agreement and allowed for identification of several model parameters (Table 1), others were taken accordingly to the literature.

4.2. Analysis of single crystal specimen – [011] case

Since DIC did not show any particular strain accumulation in the [001] and [111] experiments, a second model was developed reproducing a single crystal plate with the load direction along the [011] crystallographic direction. This analysis was performed because the DIC results revealed strain accumulation along bands during the experiments. The geometry consists of a plate (3 × 3 × 1 mm), corresponding to the central section of a dog-bone specimen. It was modeled using a mesh with average element size of 40 μm. A displacement was applied along the face (3 × 1 mm) normal to the [011] direction, and the opposing face was displacement constrained. The local behavior comparison for the [011] oriented specimen is shown in Fig. 4. To match the results, since the tensile curves have slight differences (Fig. 3b), the local behavior of the simulation was analyzed at an overall strain of 4.9%, the same as the DIC results. From the comparison, the model shows strain accumulation along 40.1° direction which is comparable with the 39° of the experiment.

5. Model validation and analyses on a polycrystalline aggregates

Having verified the parameters with the single crystal models, it was possible to analyze a polycrystalline aggregate. The simulation will emulate a specimen that undergoes a tensile test at 700 °C and with the strain field measured via high resolution *ex-situ* (Pataky and Sehitoglu, 2015). To account for the test at 700 °C some parameters were adjusted accordingly to the experimental stress-strain curve, the modified parameters are recorded in Table 2.

5.1. Finite element model of a polycrystalline specimen

The geometry of the FE model was defined by the DIC area of interest. Fig. 5 shows two micro structural maps from the EBSD analysis conducted on the specimen. The areas of Fig. 5a and c dimensions are respectively, 354 μm by 291 μm and 204 μm by

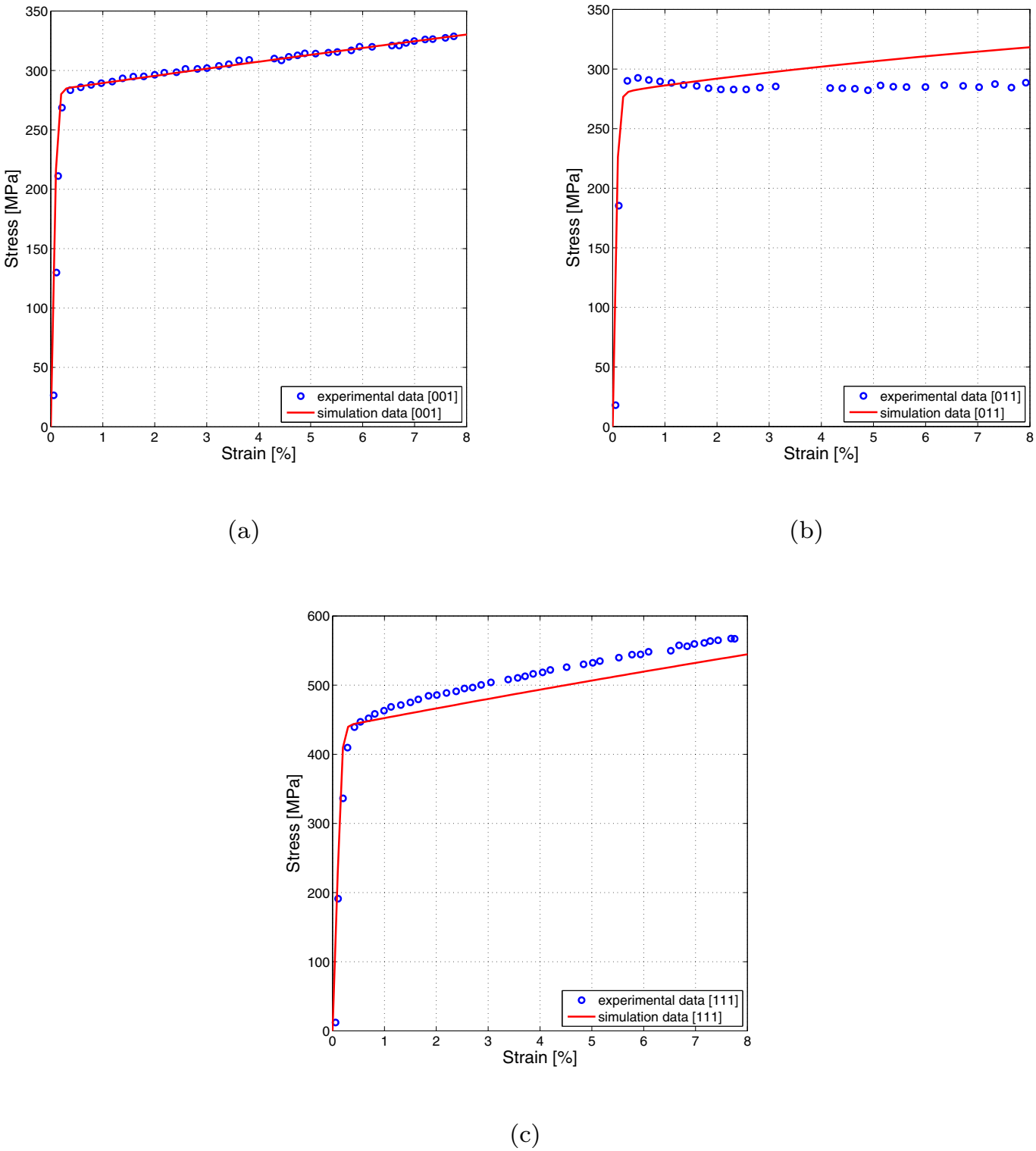

Fig. 3. Single crystal results for tensile tests, analysis of the macroscopic behavior with comparison between simulations and experiments: a) [001]; b) [011]; c) [111].

229 μm. The grains' geometries, orientations and the position of the carbides (white circles in Fig. 5a–c) were taken directly from the EBSD data (Pataky et al., 2013).

The meshing of the two models, shown in Fig. 5b and d, was done with linear hexahedral elements with an average size of 3.5 μm. Convergence testes were made, the proposed dimensions for the element granted no differences in terms of localizations and tensile curve with models where the mesh was refined further. The models were 5 elements thick (20 μm), thus the model can be considered in plane stress; the third direction was enough thin to not being considered a preferential one (like an extrusion), keeping the overall answer of the model close to isotropic. The two models consist of, respectively, about 46,000 and 23,000 elements. Fig. 5b and d also show a schematic of the loading and constraints. To simulate a tensile experiment, a displacement was applied to the nodes at the upper face, while a double symme-

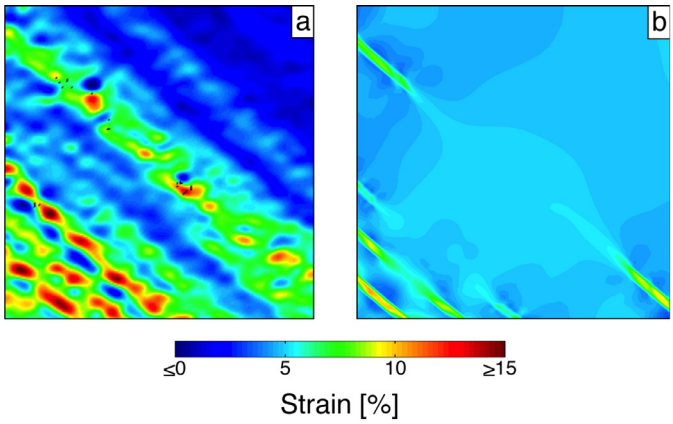

Fig. 4. [011] single crystal strain field. Comparison between the strain field obtained with DIC analysis (a) and with FE simulation (b). The strain considered is the one along the loading direction.

try was applied as shown in figures. It is clear that the simulation results of such thin reference volumes with only one layer of grains can differ from a full 3D model (Zeghadi et al., 2007). For a first assessment in the description of the localization of stresses and strains across the grains, the adoption of columnar grains can be proven valuable; considering these kind of modeling features, in Sistaninia and Niffenegger (2015) crack initiation and in Aubert et al. (2016) heterogeneities of the mechanical field were studied. This shortcoming may be taken into account in future works where a fully 3D domain, generated by subsequent polishing of the specimen or advanced EBSD technique, will be used for analogous simulations.

Table 2
Material parameters for crystal plasticity simulation of Haynes 230 polycrystalline specimen.

Property	Description	Fitting/Literature	Value
E	Young's modulus	Fitted	201 GPa
μ_0	Shear modulus	Fitted	84 GPa
$\hat{\tau}_y$	MTS strength for intrinsic barrier (yield)	Fitted	128 MPa
$\hat{\tau}_\nu$	MTS strength for work hardening	Fitted	40 MPa
ϑ_0	Initial hardening slope	Fitted	225 MPa

5.2. Comparison with experimental results

The simulation was carried out on the two areas with 3 subsequent unloads resulting in residual strains of 1.22%, 1.59% and 2.51%. Fig. 6 shows a comparison between the stress-strain curves from the experiment, measured with DIC, and those extracted from the models. A good agreement between the two was demonstrated. Global strain and stresses were obtained from the models through a volume average over the elements values. This result pointed out that both models, despite the difference in surface extension, contained enough grains to be able to describe the experimental global behavior. For the following analysis the first unloading (1.22%) will be used as a reference of the comparison with the experimental results at the micro-scale.

Fig. 7a and d are the DIC strain fields from the two considered areas, highlighting strain accumulation along grains. The first attempt in approximating these results concerned the adoption of models without carbides. Fig. 7b and e are the results obtained. They showed agreement on several grain's slip activation, but there were also many mismatches. The introduction of carbides, as identified in Fig. 5, modeled as purely elastic materials (with

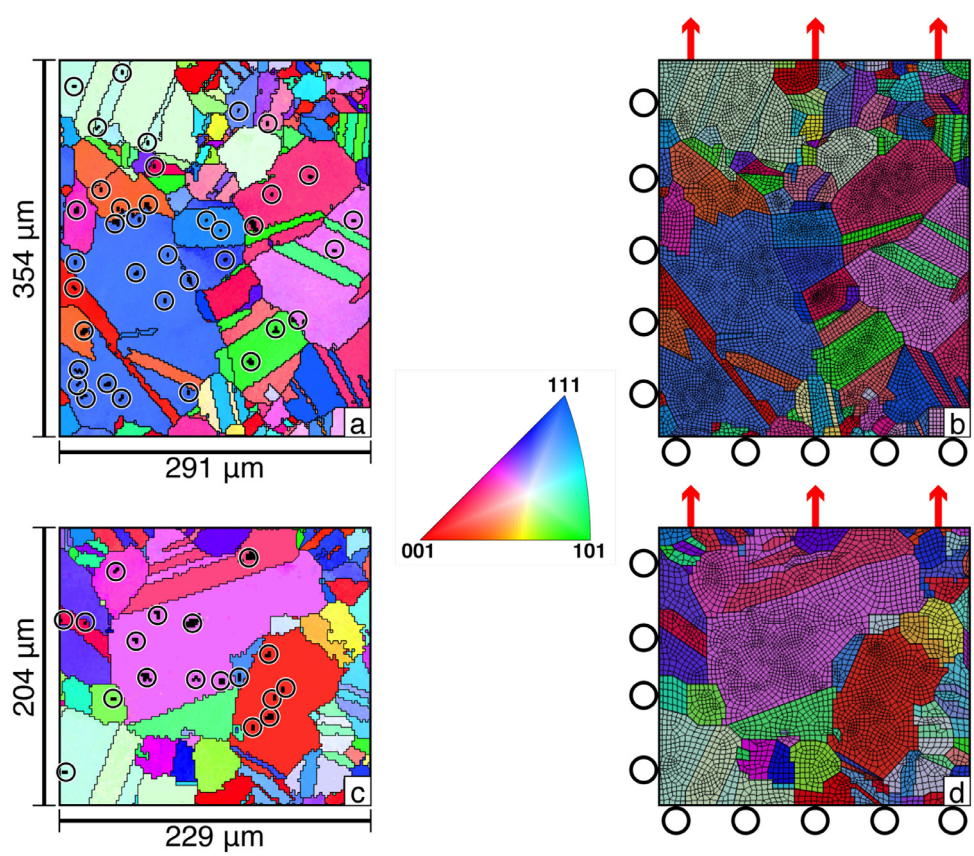

Fig. 5. Polycrystalline model for the two extracted areas (a-b is the first inspected area, c-d is the second inspected area). a) and c) are the EBSD of the two inspected areas, with evidence of grains geometry, surface dimensions and carbides identification; b) and d) are the model of the areas, with highlights on loading direction and constraints.

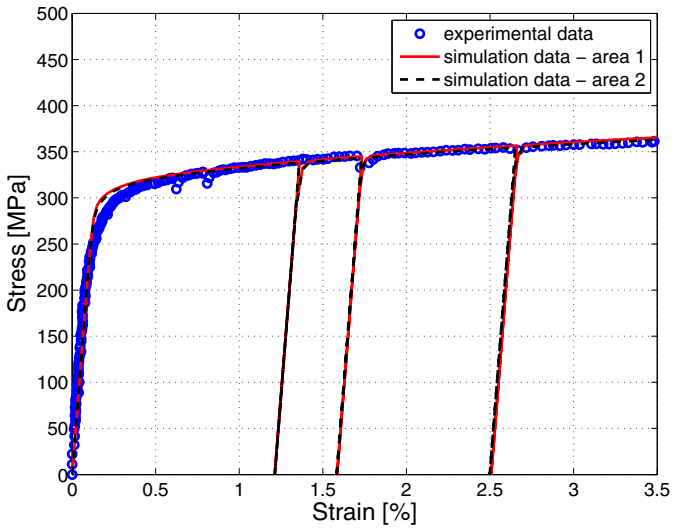

Fig. 6. Polycrystalline model: comparison between the stress-strain curves obtained with the experimental procedure and the FE analysis of area 1 and area 2 (the two simulations overcome each other).

a high elastic modulus) (Groover, 2007), had influence on the local behavior, while the stress-strain curves were consistent with those in Fig. 6. The local strain intensification, due to the carbides, reported in Fig. 7c and f, advanced the approximation of the experiment. Fig. 8 shows details of the strain field modification due to carbides presence, considering only the numerical results; the comparison is between the central portions of the models reproducing Area 1, Fig. 8 a has no carbides and Fig. 8b has the carbides (the carbide position is shown in the picture).

Fig. 9 shows the strain value distribution histograms of the model compared to the DIC. For consistency, the number of strain values sampled with DIC and the FE model had to be the same. For the first area, the DIC showed a majority of values around the average while the simulation showed a plateau. The second simulation instead showed a trend similar to the experiment, despite having a difference in 0.2% in the average strain. The difference can be

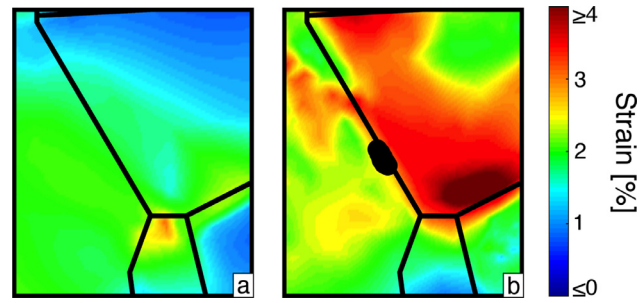

Fig. 8. Highlight of the comparison between the strain fields (a) without carbides and (b) with carbides.

associated to the fact that the model was loaded to reproduce the global behavior of the specimen, measured over the entire DIC area of interest in Pataky and Sehitoglu (2015), while locally the DIC in the second surface area registered a lower mean cumulated strain.

A section of the second model was further investigated with a line scan. Fig. 10a shows the comparison between 3 datasets: the experiment, the simulation without carbides and the simulation with carbides. It can be noted that the three curves were similar in terms of trends and magnitudes. The trends were well captured by the first simulation, considering the peaks and valleys, and improved upon by the introduction of the inclusions. In the second model, the slip traces were identified for two grains (Engler and Randle, 2010; Abuzaid et al., 2012); activated slip systems were identified by detecting the highest strain accumulation orientations. Considering the stress field at the maximum peak of the simulation stress-strain curve, before the unloading, it was possible to evaluate the local shear stress along the identified traces. These results were then compared with the value of the externally applied resolved shear stresses, Fig. 10 b, obtained from the Schmid law (Schmid and Boas, 1950):

$$\tau_{remote} = m \cdot \sigma_{remote} \tag{21}$$

where this shear stress is evaluated from the remote applied stress multiplied by the Schmid factor of the grain. This value is usually considered constant in the application of energy models for crack

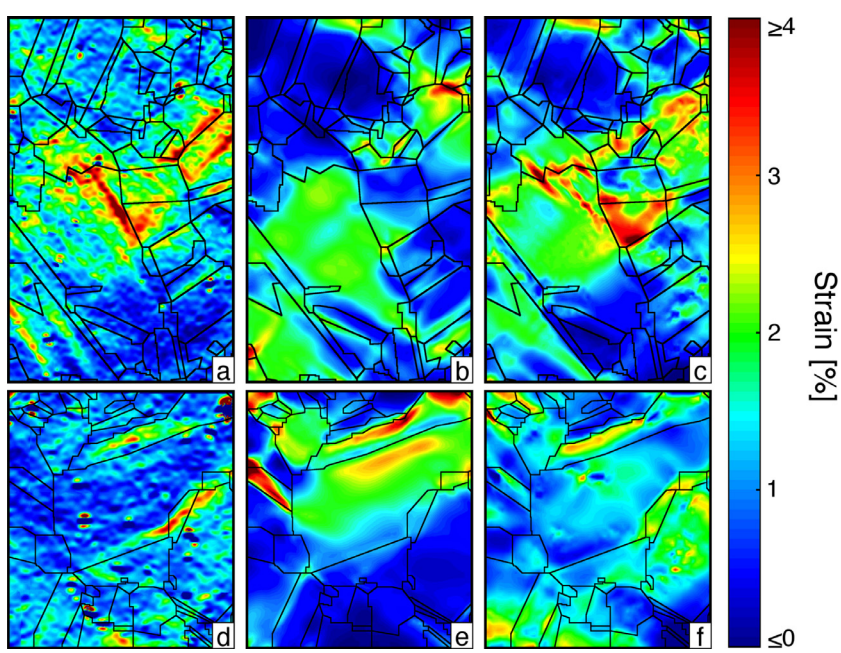

Fig. 7. Polycrystalline results for the two extracted areas, comparison of the strain fields between FE models and experiments. First area: a) DIC results; b) simulation without carbides; c) simulation with carbides. Second area: d) DIC results; e) simulation without carbides; f) simulation with carbides.

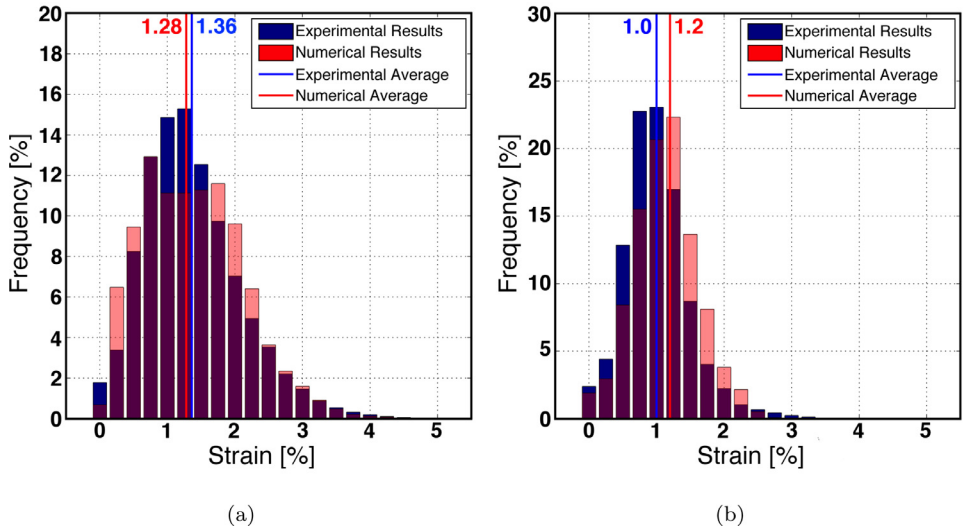

(a) (b)

Fig. 9. Histogram comparison between simulation and experimental strain distribution across the analyzed areas, with a note about the average of the two distribution: a) first area; b) second area.

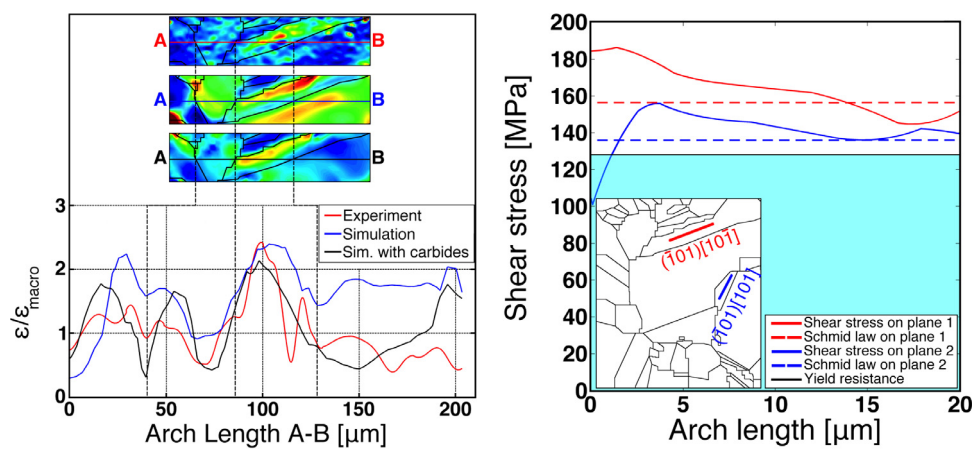

(a) (b)

Fig. 10. Investigations on second area: a) analysis and comparison of the strain field along an arch AB considering DIC, simulation without carbides and simulation with carbides; b) shear stress variation along two highlighted planes and comparison with the Schmid law.

nucleation (Sangid et al., 2011) and Fig. 10b shows that the constant values coming from the Schmid law and the local shear stress are of the same order.

In addition to the strain field, used for the comparison with the DIC, FE models allow for determination through the constitutive equations of the stress fields. Fig. 11 shows the stresses along the loading direction for the two analyzed model. Shown are the stress field at the maximum applied stress and after the unload, where the residual stresses can be estimated.

Since the model provides the Nye tensor components as an output (Healy et al., 2015), it was possible to determine the necessary dislocation density map through the relationship:

$$\rho b = \|\alpha\| = \sqrt{\alpha : \alpha} \tag{22}$$

This quantity, in Fig. 12, indicates the regions of high plastic strain incompatibility, where large densities of necessary dislocations developed to maintain the compatibility throughout the model.

6. Conclusions

Modeling results, using the Warp3D CP model, allowed for the description and the study of how the localizations of strains and stresses act on local scale level. Moreover, considering the global behavior, there is a good approximation of the stress-strain curves for both single crystal and polycrystalline specimens. Two models were created assembling grains with different sizes and orientations. The interaction of those grains, each one can be considered locally as an anisotropic system, was able to reproduce the global behavior of a specimen that on the macro-scale can be seen as homogeneous and isotropic. This result was possible since the models consisted of enough grains with different orientations to create a polycrystalline aggregate.

Finally the comparison of the strain accumulation, on the local scale, showed a good agreement in terms of active grains between the model and the experiment. The introduction of carbides improved the description of the residual strain field, showing that they have a significant role inside the material.

The shear stresses along the slip traces, obtained with the model, showed a good agreement with the approximation of the Schmid law, which considers the external shear stress evaluated with Eq. (21) as constant.

Acknowledgments

Partial support was made available from Nyquist endowment at the University of Illinois at Urbana Champaign and from the

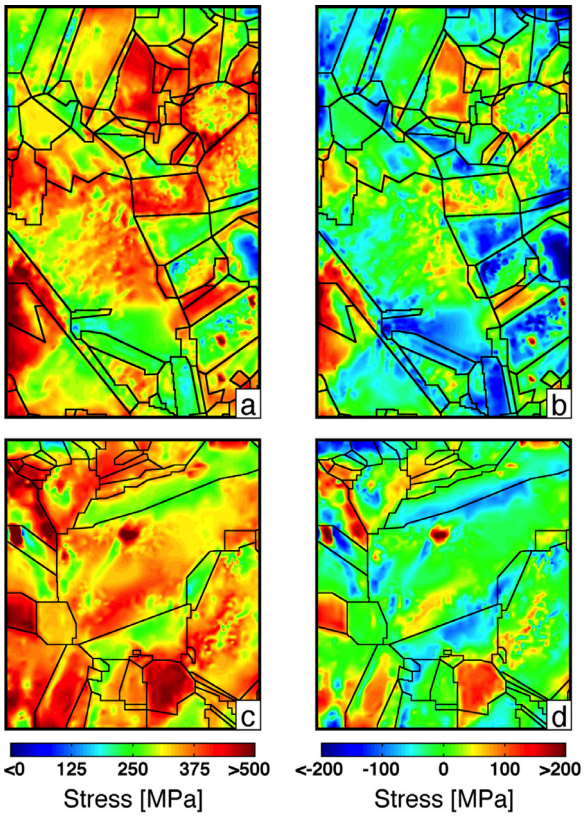

Fig. 11. Polycrystalline models results for the two extracted areas. Stress fields in the loading direction. a), c) are the stress fields at the maximum stress before the unload: a)first area, c) send area. b), d) are the stress fields after the unload at a residual strain of 1.22%: b) first area, d) second area.

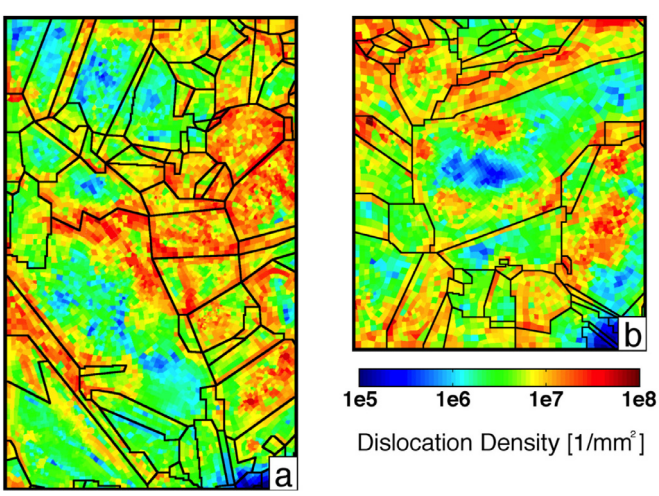

Fig. 12. Polycrystalline dislocation density maps at 1.22% average strain after the unload: a) first area; b) second area.

Doctoral School of Politecnico di Milano. Single crystals were grown by Prof. Yuri Chumlyakov (Tomsk State University-Siberian Physical Technical Institute).

References

Abuzaid, W.Z., Sangid, M.D., Carroll, J.D., Sehitoglu, H., Lambros, J., 2012. Slip transfer and plastic strain accumulation across grain boundaries in hastelloy x. J. Mech. Phys. Solids 60 (6), 1201–1220.
Acharya, A., Bassani, J., Beaudoin, A., 2003. Geometrically necessary dislocations, hardening, and a simple gradient theory of crystal plasticity. Scr. Mater. 48 (2), 167–172.
Aifantis, E., 1995. Pattern formation in plasticity. Int. J. Eng. Sci. 33 (15), 2161–2178.
Asaro, R.J., 1983. Micromechanics of crystals and polycrystals. Adv. Appl. Mech. 23 (1), 115.
Aubert, I., Saintier, N., Olive, J.-M., Plessier, F., 2016. A methodology to obtain data at the slip-band scale from atomic force microscopy observations and crystal plasticity simulations. application to hydrogen-induced slip localization on aisi 316l stainless steel. Acta Mater. 104, 9–17.
Banerjee, B., 2007. The mechanical threshold stress model for various tempers of aisi 4340 steel. Int. J. Solids Struct. 44 (3), 834–859.
Barbe, F., Decker, L., Jeulin, D., Cailletaud, G., 2001. Intergranular and intragranular behavior of polycrystalline aggregates. part 1: Fe model. Int. J. Plast. 17 (4), 513–536.
Barbe, F., Forest, S., Cailletaud, G., 2001. Intergranular and intragranular behavior of polycrystalline aggregates. part 2: results. Int. J. Plast. 17 (4), 537–563.
Diard, O., Leclercq, S., Rousselier, G., Cailletaud, G., 2005. Evaluation of finite element based analysis of 3d multicrystalline aggregates plasticity: application to crystal plasticity model identification and the study of stress and strain fields near grain boundaries. Int. J. Plast. 21 (4), 691–722.
Engler, O., Randle, V., 2010. Introduction to Texture Analysis. CRC Press, Taylor & Francis Group, FL.
Follansbee, P., 2014. Fundamentals of strength.
Follansbee, P., Kocks, U., 1988. A constitutive description of the deformation of copper based on the use of the mechanical threshold stress as an internal state variable. Acta Metall. 36 (1), 81–93.
Goto, D., Garrett Jr, R., Bingert, J., Chen, S.-R., Gray III, G.T., 2000. The mechanical threshold stress constitutive-strength model description of hy-100 steel. Metall. Mater. Trans. A 31 (8), 1985–1996.
Gray III, G.T., Chen, S.R., Vecchio, K.S., 1999. Influence of grain size on the constitutive response and substructure evolution of monel 400. Metall. Mater. Trans. A 30 (5), 1235–1247.
Groover, M.P., 2007. Fundamentals of Modern Manufacturing: Materials Processes, and Systems. John Wiley & Sons.
Healy, B., Gullerud, A., Koppenhoefer, K., Roy, A., Roy-Chowdhury, S., Petti, J., Walters, M., Bichon, B., Cochran, K., Carlyle, A., Sobotka, J., Messner, M., Dodds, R., 2015. Warp3d: 3-d dynamic nonlinear fracture analyses of solids using parallel computers, structural research series (srs 607) uilu-eng-95-2012, university of illinois at urbana-champaign.
Kocks, U., Mecking, H., 2003. Physics and phenomenology of strain hardening: the fcc case. Prog. Mater. Sci. 48 (3), 171–273.
Kocks, W., 1975. Thermodynamics and kinetics of slip. Progr. Mater. Sci. 19, 291.
Kok, S., Beaudoin, A., Tortorelli, D., 2002. On the development of stage iv hardening using a model based on the mechanical threshold. Acta Mater. 50 (7), 1653–1667.
Kok, S., Beaudoin, A., Tortorelli, D., 2002. A polycrystal plasticity model based on the mechanical threshold. Int. J. Plast. 18 (5), 715–741.
Lee, E.H., 1969. Elastic-plastic deformation at finite strains. J. Appl. Mech. 36 (1), 1–6.
Lu, Y., Chen, L., Wang, G., Benson, M., Liaw, P., Thompson, S., Blust, J., Browning, P., Bhattacharya, A., Aurrecoechea, J., et al., 2005. Hold time effects on low cycle fatigue behavior of haynes 230® superalloy at high temperatures. Mater. Sci. Eng.: A 409 (1), 282–291.
Marin, E., Dawson, P., 1998. Elastoplastic finite element analyses of metal deformations using polycrystal constitutive models. Comput. Methods Appl. Mech. Eng. 165 (1), 23–41.
Musienko, A., Tatschl, A., Schmidegg, K., Kolednik, O., Pippan, R., Cailletaud, G., 2007. Three-dimensional finite element simulation of a polycrystalline copper specimen. Acta Mater. 55 (12), 4121–4136.
Nye, J., 1953. Some geometrical relations in dislocated crystals. Acta Metall. 1 (2), 153–162.
Pataky, G.J., Sehitoglu, H., 2015. Experimental methodology for studying strain heterogeneity with microstructural data from high temperature deformation. Exp. Mech. 55 (1), 53–63.
Pataky, G.J., Sehitoglu, H., Maier, H.J., 2013. Creep deformation and mechanisms in haynes 230 at 800 c and 900 c. J. Nucl. Mater. 443 (1), 484–490.
Reu, P., 2015. Virtual strain gage size study. Exp. Tech. 39 (5), 1–3.
Roters, F., Eisenlohr, P., Hantcherli, L., Tjahjanto, D.D., Bieler, T.R., Raabe, D., 2010. Overview of constitutive laws, kinematics, homogenization and multiscale methods in crystal plasticity finite-element modeling: theory, experiments, applications. Acta Mater. 58 (4), 1152–1211.
Sangid, M.D., Maier, H.J., Sehitoglu, H., 2011. The role of grain boundaries on fatigue crack initiation–an energy approach. Int. J. Plast. 27 (5), 801–821.
Schmid, E., Boas, W., 1950. Plasticity of crystals.
Sistaninia, M., Niffenegger, M., 2015. Fatigue crack initiation and crystallographic growth in 316l stainless steel. Int. J. Fatigue 70, 163–170.
Xie, C., Ghosh, S., Groeber, M., 2004. Modeling cyclic deformation of hsla steels using crystal plasticity. J. Eng. Mater. Technol. 126 (4), 339–352.
Zbib, H.M., de la Rubia, T.D., 2002. A multiscale model of plasticity. Int. J. Plast. 18 (9), 1133–1163.
Zeghadi, A., N'guyen, F., Forest, S., Gourgues, A.-F., Bouaziz, O., 2007. Ensemble averaging stress–strain fields in polycrystalline aggregates with a constrained surface microstructure–part 1: anisotropic elastic behaviour. Philos. Mag. 87 (8–9), 1401–1424.